Structure, stability and work functions of the low index surfaces of pure indium oxide and Sn-doped indium oxide (ITO) from density functional theory†

Aron Walsh* and C. Richard A. Catlow

Indium sesquioxide is a transparent conducting oxide material widely used in photovoltaic and solid-state lighting devices. We report a study of the surface properties of the thermodynamically stable bixbyite phase of In_2O_3 using density functional theory. The surface energies follow the order $\gamma(100) > \gamma(110) > \gamma(111)$, with the charge neutral (111) termination being the lowest energy cleavage plane. The surface work functions (vertical ionisation potentials) are calculated using a non-local hybrid density functional, and show good agreement with recent experimental measurements. Finally, SnO_2 doping of the (111) surface is presented, where the Sn substitutions are more favourable on the surface sites and the excess electrons are delocalised amongst the In_2O_3 conduction states; the enthalpy of solution is estimated to be 60 kJ mol^{-1}.

1. Introduction

Indium oxide has long been of interest as a transparent conducting oxide,[1–3] combining optical transparency in the visible range with conductivity approaching that of a metal. Despite its wide range of applications including solar cell and inorganic lighting devices, and detailed investigations of the bulk defect and electrical properties,[2,4–9] its surface chemistry has been largely ignored due to a combination of its complex crystal structure and the difficulty in growing high-quality single crystals. In the past number of years, there has been a renewed interest in the basic material properties of In_2O_3 and Sn-doped In_2O_3 (ITO), with recent studies including epitaxial growth of single crystals on cubic zirconia substrates;[10–12] measurement of the work function and interfacial properties of polycrystalline samples;[13,14] and scanning-tunnelling microscopy (STM) of the (111) and (100) terminated surfaces.[15,16] As ITO is currently the leading cathode material in organic solar cell and light emission devices, improved understanding of its surface properties is required to understand and further improve the interfacial charge transfer processes,[17] in addition to suggesting alternative cathode materials.

The thermodynamically stable phase of In_2O_3 is the body-centred cubic bixbyite crystal structure, which contains 80 atoms in the unit cell. While bixbyite is a common sesquioxide crystal structure (*e.g.* Tl_2O_3, Er_2O_3 and Y_2O_3),[18,19] the surface chemistry of bixbyite crystals has not been well characterised due to its inherently complex structure. However, bixbyite can be viewed in terms of a simpler face-centred cubic fluorite (CaF_2) $2 \times 2 \times 2$ supercell with one quarter of the anion sites vacant, as illustrated in Fig. 1. We can therefore use the extensive knowledge of the surface chemistry of fluorite structured crystals[20] to provide some initial insights into the more complex bixbyite based systems.

Density functional theory (DFT) has become an essential tool in the atomistic characterisation of metal oxide surfaces;[21–29] unfortunately, surface investigations of In_2O_3 have been limited until very recently. Fuks *et al.*[30] studied the (110) surface using DFT; however, no energetics or surface structures were reported. Xiao *et al.*[31] predicted "d⁰" magnetism on the non-stoichiometric polar (100) surface due to (unphysical) uncompensated electrical
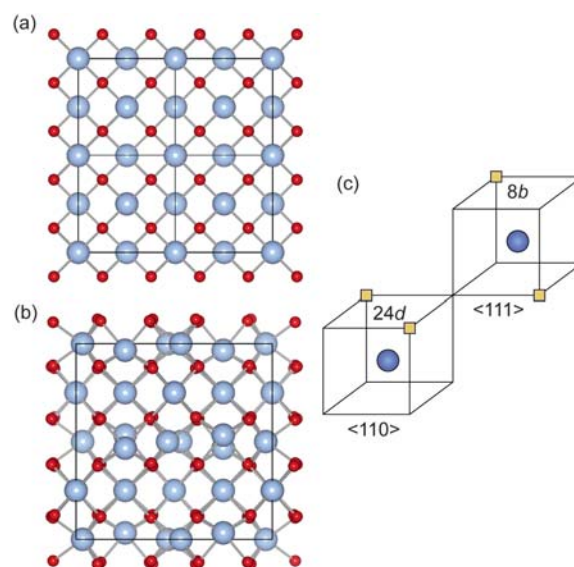

Fig. 1 Crystal structure representations of (a) a fluorite structured (AB_2) $2 \times 2 \times 2$ supercell and (b) a bixbyite structured (A_2B_3) unit cell. The structural anion vacancy configurations around both types of cation sites (8b $\left(\frac{1}{4}, \frac{1}{4}, \frac{1}{4}\right)$ and 24d $\left(u, 0, \frac{1}{4}\right)$ Wyckoff positions) in bixbyite are shown in (c). The cations are coloured blue (large balls), with red anions (small balls).

Materials Chemistry, Department of Chemistry, University College London, 3rd Floor, Kathleen Lonsdale Building, Gower Street, London, WC1E 6BT, UK. E-mail: a.walsh@ucl.ac.uk
† This paper is part of a *Journal of Materials Chemistry* themed issue on Modelling of Materials. Guest editors: Julian Gale and Mark Wilson.

charging, but again the details of the surface structure and stability were not considered. In the work of Golovanov et al.[32] reconstructions of the oxygen terminated (100) surfaces were investigated, indicating a decrease in the surface energy through dimerisation of the exposed oxygen atoms. A combined theoretical and experimental investigation of the (111) surface identified a simple (1 × 1) surface termination, as supported through STM measurements and DFT simulations. In contrast, computational studies of the defect processes occurring in the bulk material have been more abundant,[6–9,33–35] focusing on the role of electron donating point defects such as oxygen vacancies and indium interstitials.

In this study, we present an investigation of the (100), (110) and (111) low index surfaces of In$_2$O$_3$. The surface chemistry of fluorite, and defective fluorite materials such as Y-stabilised ZrO$_2$ is found to be closely related to that of the fluorite-related bixbyite structure adopted by In$_2$O$_3$, with the surface energies following the order $\gamma(100) > \gamma(110) > \gamma(111)$. The surface work functions (vertical ionisation potentials) are found to be sensitive to the termination, varying by up to 0.7 eV. Sn substitutions on the thermodynamically favoured (111) termination are found to have a energetic preference for surface sites and result in delocalised conduction states typical of a shallow electron donor.

2.   Methods

Total energy electronic structure calculations were performed using DFT[36,37] with a plane wave basis set as implemented in the VASP package.[38,39] The semi-core 4d^{10} states of In were treated explicitly as valence within the scalar-relativistic projector augmented wave approach.[40] For the bulk cubic unit cell of In$_2$O$_3$, a 3 × 3 × 3 Monkhorst–Pack[41] k-point mesh was used together with a well converged 500 eV plane wave cut-off. Exchange-correlation effects were treated within the generalised gradient approximation (the PBE functional[42]).

The surfaces of In$_2$O$_3$ were modelled as 2D slabs within periodic boundary conditions, with a 20 Å vacuum region separating the repeating images; an alternative approach, which avoids artificial periodicity, is the multi-region embedded cluster technique, such as implemented in the ChemShell package.[28,43] For the surface calculations, equivalent k-point sampling to the bulk cell was used in-plane to ensure convergence in the total energies, with a single k-point normal to the surface slab.

While standard DFT exchange-correlation functionals, such as the PBE functional employed in this study, result in reliable predictions of ground-state properties, the electronic band gaps of insulators are underestimated at this level of theory,[44,45] which will result in spurious errors in the calculated work functions, as the proportion of correction attributable to the valence and conduction bands is unknown. To address this issue, we employ a hybrid exchange-correlation functional, which modifies the PBE functional to include 25% non-local Hartree–Fock exact-exchange.[46,47] The resulting HSE06[48] functional, which contains a screening of $\omega = 0.11$ bohr^{-1} to partition the Coulomb potential into short-range (SR) and long-range (LR) terms follows the form:

$$E_{xc}^{HSE}(\omega) = E_x^{HSE,SR} + E_x^{PBE,LR} + E_c^{PBE},$$

where

$$E_{xc}^{HSE,SR} = \frac{1}{4} E_x^{Fock,SR} + \frac{3}{4} E_x^{PBE,SR}.$$

Approaches based on hybrid functionals demonstrated early success in describing the magnetic and electronic properties of transition metal oxides,[49–52] and have had more recent application to the optical and defect properties of metal oxides[33,53–55] and chalcogenides.[46,56–58] At this level of theory, the band gap of In$_2$O$_3$ is found to be 2.7 eV, so that no further a posteriori band gap correction is necessary for a qualitative analysis. Due to the prohibitive computational expense of this approach for the large system sizes studied (>1400 valence electrons) arising from the explicit two-electron integrals, static HSE06 calculations are performed on the fully relaxed PBE surface geometries.

3.   Results and discussion

3.1   Surface chemistry of fluorite structured crystals

For single crystals of fluorite structured materials such as UO$_2$ and ThO$_2$, (111) is the natural cleavage plane, which can be understood from consideration of its low index surfaces.[20] Charged anion and cation layers are stacked along the $\langle 100 \rangle$ direction, resulting in a permanent electrical dipole for the (100) surface, which will be subject to reconstruction to quench the associated divergence in the surface energy as a function of the slab thickness. Utilising the notation of Tasker for ionic surfaces,[59] the (100) termination can be classified as a type III polar surface. In contrast, both the (110) and (111) surfaces have non-polar terminations. Layers of charge neutral layers are stacked along $\langle 110 \rangle$, resulting in a type I surface termination. Layers of anions and cations are stacked along $\langle 111 \rangle$, but these occur in charge neutral B^{1-}–A^{2+}–B^{1-} units, resulting in a type II quadrupolar termination.

Hartree–Fock calculations have been used to examine the (111) and (110) surfaces of CeO$_2$ and ZrO$_2$, with surface energies of 1.25 and 1.49 J m^{-2} reported for the (111) termination and 2.11 and 2.41 J m^{-2} for the (110) termination, respectively.[29] More recent studies of Y-doped ZrO$_2$ surfaces showed that the energetic ordering preferences of ZrO$_2$ were maintained even for high Y concentrations, where charge compensation for the negatively charged cation substitution (Y$_{Zr}'$) is achieved through the formation of oxygen vacancies (V$_O^{\bullet\bullet}$), resulting in a partially occupied oxygen sublattice similar to bixbyite,[60] i.e.

$$Y_2O_3 \xrightleftharpoons{(ZrO_2)} 2Y'_{Zr} + V_O^{\bullet\bullet} + 3O_O$$
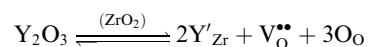
3.2   Bixbyite surfaces

As the bixbyite mineral structure represents an ordered structural vacancy superlattice of the fluorite structure, as illustrated in Fig. 1, the low index surfaces are similar in both cases. The (100) bixbyite termination remains a type III polar surface. To suppress the dipole, we perform a basic reconstruction involving a shift of half the terminating atoms from the top to the bottom of the repeating unit;[23,61] such micro-faceting has been observed to stabilise (100) terminated fluorite structured UO$_2$.[62] The

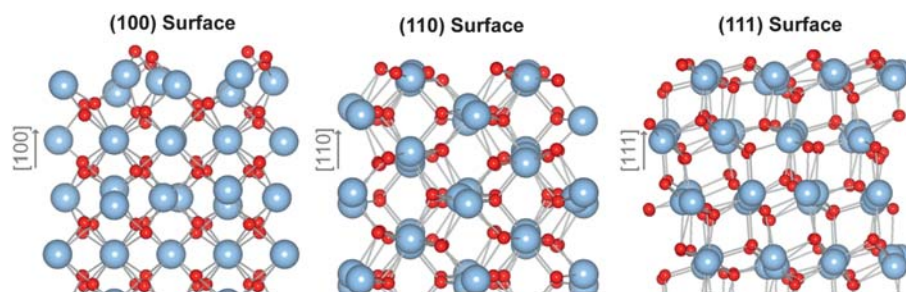**(100) Surface** **(110) Surface** **(111) Surface**

Fig. 2 Atomic representations of the top layers of the three low index surfaces of In$_2$O$_3$, relaxed using density functional theory calculations. Indium is coloured blue (large balls), with red reserved for oxygen (small balls).
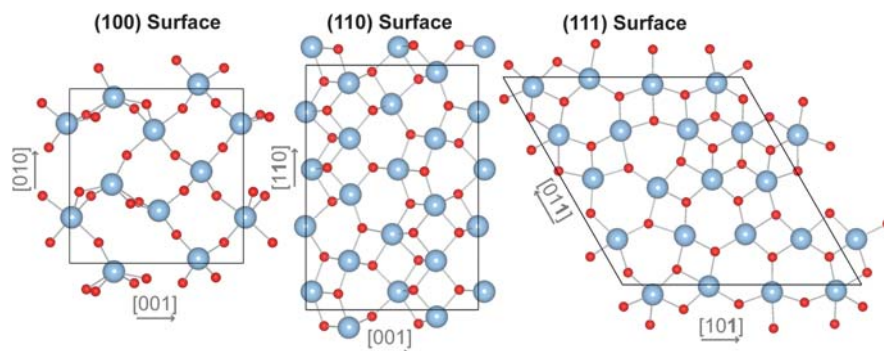
(100) Surface **(110) Surface** **(111) Surface**

Fig. 3 Projection of the first ionic layer of the three low index surfaces of In$_2$O$_3$ through the surface normal. Indium is coloured blue (large balls), with red reserved for oxygen (small balls).

faceted surface gives rise to the possibility of oxygen or indium termination, and both configurations have been explored. In contrast, the (110) and (111) surfaces are essentially non-polar and feature stoichiometric layers of In and O ions oriented perpendicular to the slab. Representations of the three surface terminations are shown in Fig. 2 and 3. As with the fluorite structured crystals, natural cleavage of bixbyite crystals in the (111) plane can be expected to arise from the double layer of oxygen anions present between the charge neutral repeating O_{12}^{2-}–In_{16}^{3+}–O_{12}^{2-} units in the $\langle 111 \rangle$ direction.

The surface energy is defined as the energy per unit area required for forming the surface relative to the bulk, and is calculated according to:

$$\gamma = \frac{U_{\text{slab}} - U_{\text{bulk}}}{2 \times A},$$

where U_{slab} is the total energy of the 2D slab with a 20 Å vacuum region and U_{bulk} is the energy of the corresponding amount of bulk In$_2$O$_3$ units. A represents the surface area, which is created on each side of the 2D slab and is repeated periodically. For

bixbyite In$_2$O$_3$ (experimental lattice constant $a = 10.117$ Å[63]), the areas of the (100), (110) and (111) low index surfaces studied are $a \times a = 102.35$ Å^2, $a \times a\sqrt{2} = 144.75$ Å^2 and $a\sqrt{2} \times a\sqrt{2} \times \left(\sqrt{3}/2 \right) = 177.28$ Å^2, respectively.

The calculated energies, from explicit density functional theory calculations, are listed in Table 1 for both the bulk terminated and relaxed low index surfaces. The 2D slab models for the (100), (110) and (111) surfaces contain 32 (eight cationic layers), 32 (eight cationic layers), and 48 (six cationic layers) formula units, respectively. In each case, the top two surface layers were relaxed, so that the atomic forces reduced to below 0.01 eV Å^{-1}, while the atoms at the centre of the slab were fixed at the their equilibrium bulk positions to maintain the bulk lattice spacing. The (111) surface is energetically favoured over the (110) surface by 0.179 J m^{-2}, which compares to differences of 0.12–0.46 J m^{-2} for UO$_2$ at various levels of theory.[21] Both ion terminations for the reconstructed (100) surface result in a much higher energetic cost for formation, with the oxygen terminated surface being lower in energy by more than 0.3 J m^{-2}. The surface relaxation energy is similar in all cases—of the order of 0.6 J m^{-2}—which is associated with concerted layer breathing due to the loss of atomic coordination, rather than significant surface reconstructions.

A preference for oxygen termination of the (100) surface has been also observed in recent experiments,[15] where the surface is considered to be stabilized through oxygen dimerisation.[15,32] A calculated (100)$_O$ surface energy of 2.4–1.6 J m^{-2} has been reported, depending on the surface reconstruction;[32] however, it should be noted that the slab and vacuum thickness used in the present study are double those used by Golovanov et al.,[32] so the results should only be compared qualitatively. The low surface

Table 1 Frozen and relaxed surface energies for the low index surface terminations of bixbyite In$_2$O$_3$. All values are in J m^{-2}

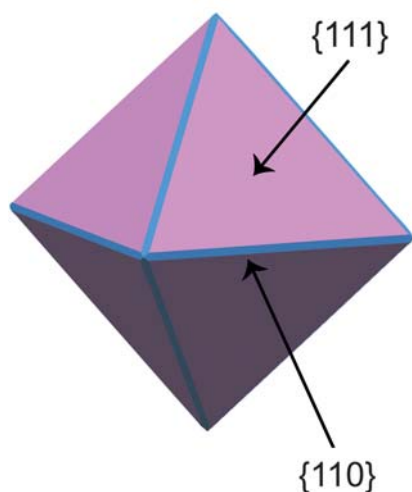|	Bulk-terminated surface energy	Relaxed surface energy	Relaxation energy
(100) In terminated	2.721	2.088	0.633
(100) O terminated	2.449	1.759	0.690
(110)	1.595	1.070	0.525
(111)	1.522	0.891	0.631

Fig. 4 Ideal crystal morphology of In_2O_3 predicted from a Wulff construction using the calculated density functional theory surface energies.

energy of the (111) termination explains recent findings that the {111} facets spontaneously form on the (100) surface.[10,12,64] In particular, growth of (100) oriented In_2O_3 films through molecular beam epitaxy recently revealed the formation of micrometre sized arrays (nanocubes) on the surface, with a clear propensity for {111} facets.[10,12] The equilibrium crystal morphology, calculated from a Wulff construction[65] using our predicted surface energies, reveals a square bipyramid constructed of {111} faces with {110} edges as shown in Fig. 4; these surface energies have also been successful in explaining the observed morphology of a range of In_2O_3 nanostructures.[66]

3.3 Surface electronic structure

The electronic density of states (EDOS) for the three stable surface terminations are shown in Fig. 5. In each case the essential features remain constant: the valence band is dominated by O 2p derived states, with a lower valence band peak (ca. −6 eV) and the conduction band states dominated by In 5s. Additional hybridisation of In 4d and 5p states in the valence band is also evident, consistent with previous analysis for the bulk material.[67] Between the three low index terminations, the only significant difference in the distribution of electronic states is observed for the $(100)_O$ surface, where the reduced coordination environment of the surface terminated oxygen atoms gives rise to a split off feature in the O 2p partial EDOS at the top of the valence band; however, these states are fully occupied and an insulating band gap is maintained. The surface EDOS features are highlighted in the plot of the spatial distribution of the highest occupied and lowest unoccupied surface states of the (111) termination shown in Fig. 6: the highest energy occupied states are associated with surface oxygen atoms, while the bottom of the conduction band is delocalised around the indium sites.

Surface states reduce the bulk band gap by 0.31–1.04 eV depending on the specific termination. Calculations performed
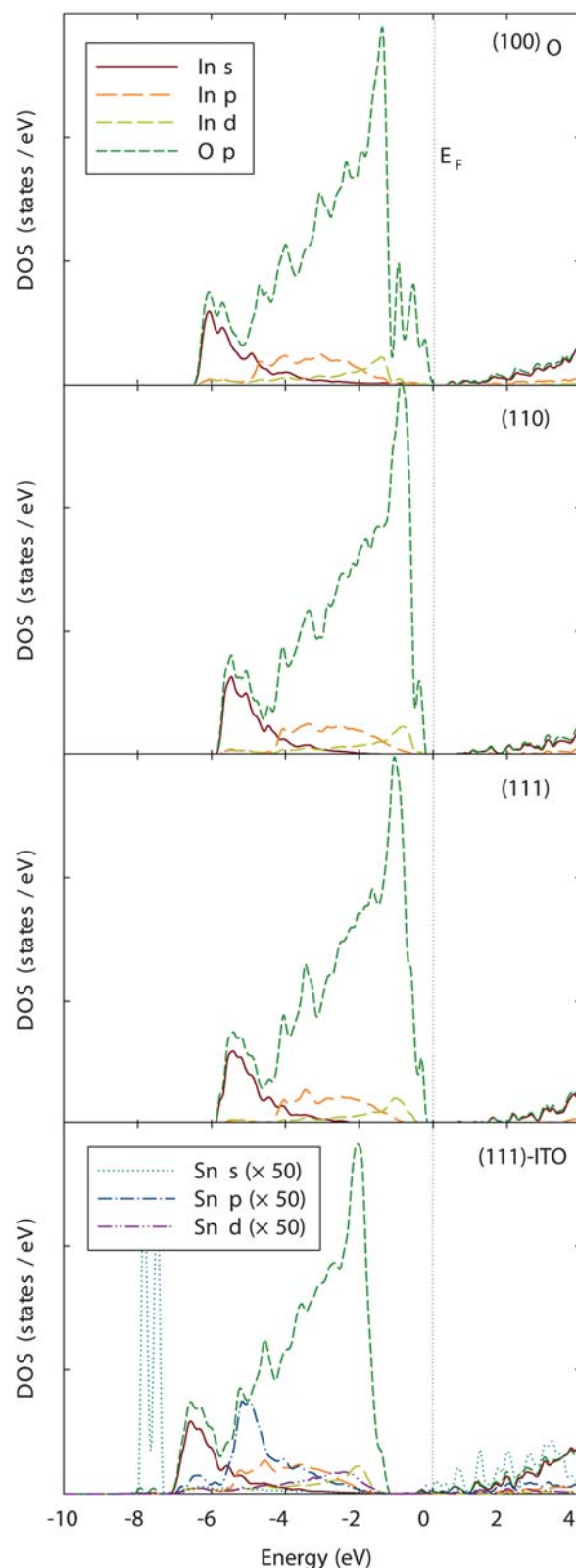

Fig. 5 Partial electronic density of states for the $(100)_O$, (110), (111) and Sn-doped (111) surfaces of In_2O_3. The highest occupied state is indicated by the dotted horizontal line, labelled E_F.
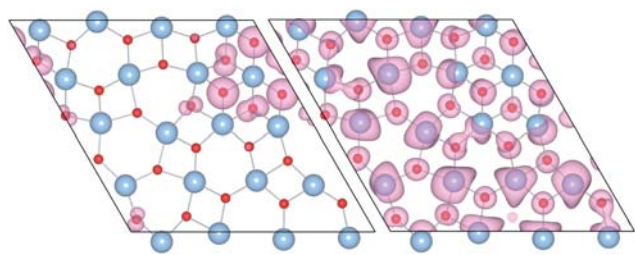
Fig. 6 Electron density isosurfaces for the lowest unoccupied (left panel) and highest occupied (right panel) states of the (111) terminated surface of In_2O_3; the isosurfaces are drawn at 1 me $Å^{-3}$ and are plotted through the surface normal.

using the hybrid HSE06 functional reveal the same trend as the semi-local functional and result in a rigid shift of the calculated PBE band gaps by 1.6 ± 0.1 eV, through both a lowering of the valence band states and a raising of the conduction band states. The resulting final band gap estimations are 1.66 eV, 2.39 eV and 2.19 eV for the $(100)_O$, (110) and (111) surfaces, respectively. The large reduction observed for the $(100)_O$ surface is directly related to the low binding energy O 2p feature produced at the top of the valence band (Fig. 5).

3.4 In_2O_3 surface potentials

The surface potentials of TCOs are of direct importance for determining their suitability for device applications, *e.g.* for maximising photovoltages in solar cells. Recent work by Klein *et al.*[13] reported the work functions measured by photoelectron spectroscopy for a range of polycrystalline TCO thin films, including In_2O_3. Considering that under most circumstances In_2O_3 is a degenerate n-type material, where the Fermi level is situated inside the conduction band, one must be careful in extrapolating from the measured work function of the doped material to the intrinsic ionisation potential associated with the upper valence band. By varying the deposition conditions and taking into account the revised electronic band gap of In_2O_3 of the order of 2.9 eV,[68] Klein *et al.* reported a value of 7.1 eV for the ionisation potential of the polycrystalline material.[13]

For all surface models studied, the vacuum spacing is sufficiently large such that the planar averaged electrostatic potential converges to a constant value far from the surface. The

converged value of the electrostatic potential is taken as the reference vacuum level to which the single-particle Kohn–Sham eigenvalues are aligned. The calculated surface potentials are shown in Fig. 7, with ionisation potentials of 7.94, 6.69 and 7.22 eV for the $(100)_O$, (110) and (111) surfaces. The arithmetic mean of 7.3 eV is in remarkably good agreement with the value of 7.1 eV reported by Klein *et al.* Importantly, the present results suggest that varying the surface morphology should offer a way to tune the surface potentials: the ionisation potential of the reconstructed (100) surface is largest (7.94 eV), with the (110) surface smallest (6.69 eV). It should be noted that our calculations refer to the vertical ionisation potentials (excluding atomic relaxation);[69] for metal oxides with relatively localised valence bands centred on the O 2p orbitals, charge trapping to produce a localised polaronic state may result in a substantially different value for the adiabatic ionisation potential.

3.5 Sn-doped In_2O_3

As mentioned in the Introduction, further increases in the conductivity of the intrinsically n-type In_2O_3 are effected by Sn-doping, and indeed ITO is the system of choice for many optoelectronic applications.[1] A recent combined DFT and photoemission study of ITO for a range of Sn concentrations established a consistent picture of the change in electronic structure of the bulk material upon the substitution of Sn on the In sites: a new feature relating to occupied Sn 5s states emerges at the bottom of the upper valence band, while the conduction band, composed of the nominally empty In and Sn 5s orbitals, becomes occupied by the excess electrons,[67] *i.e.*

$$2SnO_2 \xrightleftharpoons{(In_2O_3)} 2Sn_{In}^{\cdot} + 2e' + 3O_O + \frac{1}{2}O_2(g)$$
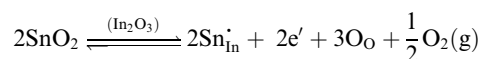
Due to the high technological importance of this system, we will now address the incorporation of Sn on the thermodynamically favoured (111) surface termination. Here, the Sn substitution is electronically compensated; ionic compensation through the formation of oxygen interstitials is known to take place for higher concentrations of Sn doping,[5] and is likely to occur through oxygen exchange with the local environment, but the relationship between the surface morphology and $p(O_2)$ is beyond the scope of the present work.

The incorporation of two substitutional Sn ions was considered on both surface and subsurface sites, which is performed on both sides of the repeating slab to avoid the formation of spurious periodic dipoles. Replacement of the lower coordination surface In sites is favoured by 0.2 eV, with no strong energetic preference between the crystallographically unique indium surface sites. The enthalpy of solution for SnO_2 incorporation into the surface, with electronic compensation, can be calculated from:

$$E_{solution} = \frac{1}{2}\Big(E_{slab}[\text{defective}] + E[In_2O_3]$$

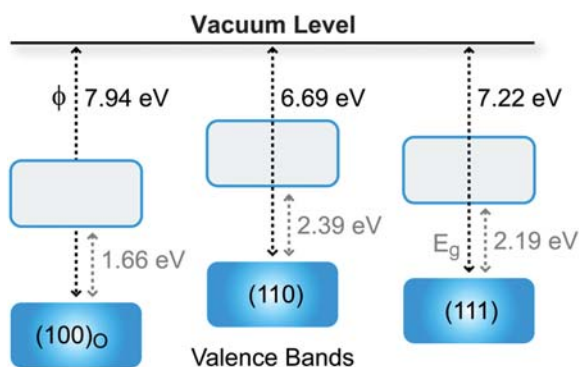$$+ \frac{1}{2}E[O_2] - E_{slab}[\text{pure}] - 2E[SnO_2]\Big),$$

Fig. 7 In_2O_3 surface ionisation potentials (work functions) and band gaps as calculated using a non-local hybrid density functional.

which contains contributions from the pure and defective slabs, as well as the total energies of gaseous dioxygen (in the ground-state triplet spin configuration), bulk bixbyite In_2O_3 and bulk rutile SnO_2. The most stable ITO surface configuration results in a solution enthalpy of 0.62 eV per Sn substitution (60 kJ mol^{-1}), which includes the cost of the excess electron in the conduction band of In_2O_3. The remarkably low value for the enthalpy is consistent with the established high solubility of Sn in the In_2O_3 lattice.

As is the case for the bulk substitution, the excess electron arising from the aliovalent Sn-substiution is delocalised over the cell, resulting in a charge distribution that is similar to the unperturbed conduction band shown in Fig. 6. The EDOS for the ITO (111) surface confirms the emergence of a new feature of mixed Sn 5s–O 2p character at −7 eV, below the onset of the In_2O_3 upper valence states, as well as the degenerate occupation of the conduction band due to the excess electrons, $i.e.$ the Fermi level lies within the conduction band. It should be noted that the delocalisation of the conduction states is not an artefact of the semi-local functional employed; indeed, in contrast to chemical reductions involving localised d states ($e.g.$ Ti(IV) to Ti(III)[24,70,71]) or f states ($e.g.$ Ce(IV) to Ce(III)[26,72]), for s states the electron self-interaction does not play a dominant role, which we have demonstrated in our hybrid density functional studies of multi-component[53] and amorphous[73] indium oxides. The ITO model surface exhibits all the key features expected for this system, and therefore provides a robust platform for future investigations of ITO surface reactions and material interfaces relevant to modern devices.

4. Conclusions

The low index surfaces of In_2O_3 have been characterised using density functional theory. The calculations indicate that the (111) surface is the thermodynamically favoured termination with a relaxed surface energy of 0.89 J m^{-2}; the reconstructed (100) surface lies 0.87 J m^{-2} higher in energy. Analysis of the work functions, performed using a hybrid density functional, is found to produce surface potentials that are in good agreement with recent experiments, and indicates a significant surface dependence of the ionisation potentials, which may be important in device applications of the material. Finally, Sn-doping of the stable (111) surface indicated an energetic preference for the surface sites, with a solution enthalpy of 0.62 eV per Sn substitution. In conclusion, our study has given valuable insights into the surface terminations of In_2O_3 $in vacuo$; future studies should address the effects of the chemical environment on the surface, where exchange of oxygen resulting in non-stoichiometry is likely to occur.

Acknowledgements

References

1 C. G. Granqvist and A. Hultaker, *Thin Solid Films*, 2002, **411**, 1.
2 J. H. W. De Wit, *J. Solid State Chem.*, 1973, **8**, 142–149.
3 P. P. Edwards, A. Porch, M. O. Jones, D. V. Morgan and R. M. Perks, *Dalton Trans.*, 2004, 2995–3002.
4 J. H. W. De Wit, *J. Solid State Chem.*, 1977, **20**, 143–148.
5 G. Frank and H. Köstlin, *Appl. Phys. A: Mater. Sci. Process.*, 1982, **27**, 197–206.
6 I. Tanaka, F. Oba, K. Tatsumi, M. Kunisu, M. Nakano and H. Adachi, *Mater. Trans.*, 2002, **43**, 1426–1429.
7 P. Agoston and K. Albe, *Phys. Chem. Chem. Phys.*, 2009, **11**, 3226–3232.
8 A. Walsh, C. R. A. Catlow, A. A. Sokol and S. M. Woodley, *Chem. Mater.*, 2009, **21**, 4962–4969.
9 S. Lany and A. Zunger, *Phys. Rev. Lett.*, 2007, **98**, 045501–045504.
10 A. Bourlange, D. J. Payne, R. G. Egdell, J. S. Foord, P. P. Edwards, M. O. Jones, A. Schertel, P. J. Dobson and J. L. Hutchison, *Appl. Phys. Lett.*, 2008, **92**, 092117.
11 P. D. C. King, T. D. Veal, D. J. Payne, A. Bourlange, R. G. Egdell and C. F. McConville, *Phys. Rev. Lett.*, 2008, **101**, 116808.
12 A. Bourlange, D. J. Payne, R. M. J. Jacobs, R. G. Egdell, J. S. Foord, A. Schertel, P. J. Dobson and J. L. Hutchison, *Chem. Mater.*, 2008, **20**, 4551–4553.
13 A. Klein, C. Körber, A. Wachau, F. Säuberlich, Y. Gassenbauer, R. Schafranek, S. P. Harvey and T. O. Mason, *Thin Solid Films*, 2009, **518**, 1197.
14 Y. Gassenbauer, A. Wachau and A. Klein, *Phys. Chem. Chem. Phys.*, 2009, **11**, 3049–3054.
15 E. H. Morales and U. Diebold, *Appl. Phys. Lett.*, 2009, **95**, 3.
16 E. H. Morales, Y. He, M. Vinnichenko, B. Delley and U. Diebold, *New J. Phys.*, 2008, **10**, 125030.
17 N. R. Armstrong, P. A. Veneman, E. Ratcliff, D. Placencia and M. Brumbach, *Acc. Chem. Res.*, 2009, **42**, 1748–1757.
18 C. T. Prewitt, R. D. Shannon, D. B. Rogers and A. W. Sleight, *Inorg. Chem.*, 1969, **8**, 1985.
19 P. A. Glans, T. Learmonth, K. E. Smith, J. Guo, A. Walsh, G. W. Watson, F. Terzi and R. G. Egdell, *Phys. Rev. B: Condens. Matter Mater. Phys.*, 2005, **71**, 235109.
20 P. A. Cox, *The Surface Science of Metal Oxides*, Cambridge University Press, Cambridge, 1994.
21 F. N. Skomurski, R. C. Ewing, A. L. Rohl, J. D. Gale and U. Becker, *Am. Mineral.*, 2006, **91**, 1761–1772.
22 M. Digne, P. Sautet, P. Raybaud, P. Euzen and H. Toulhoat, *J. Catal.*, 2002, **211**, 1–5.
23 D. O. Scanlon, A. Walsh, B. J. Morgan, M. Nolan, J. Fearon and G. W. Watson, *J. Phys. Chem. C*, 2007, **111**, 7971–7979.
24 B. J. Morgan and G. W. Watson, *Surf. Sci.*, 2007, **601**, 5034.
25 J. A. Enterkin, A. K. Subramanian, B. C. Russell, M. R. Castell, K. R. Poeppelmeier and L. D. Marks, *Nat. Mater.*, 2010, **9**, 245–248.
26 M. Nolan, S. Grigoleit, D. C. Sayle, S. C. Parker and G. W. Watson, *Surf. Sci.*, 2005, **576**, 217–229.
27 G. Henkelman, B. P. Uberuaga, D. J. Harris, J. H. Harding and N. L. Allan, *Phys. Rev. B: Condens. Matter Mater. Phys.*, 2005, **72**, 115437.
28 A. A. Sokol, S. T. Bromley, S. A. French, C. R. A. Catlow and P. Sherwood, *Int. J. Quantum Chem.*, 2004, **99**, 695–712.
29 S. Gennard, F. Cora and C. R. A. Catlow, *J. Phys. Chem. B*, 1999, **103**, 10158–10170.
30 D. Fuks, D. Shapiro, A. Kiv, V. Golovanov and C.-C. Liu, *Int. J. Quantum Chem.*, 2010, DOI: 10.1002/qua.22487, in press.
31 Z. R. Xiao, X. F. Fan, L. X. Guan, C. H. A. Huan, J. L. Kuo and L. Wang, *J. Phys.: Condens. Matter*, 2009, **21**, 272202.
32 V. Golovanov, M. A. Mäki-Jaskari, T. T. Rantala, G. Korotcenkov, V. Brinzari, A. Cornet and J. Morante, *Sens. Actuators, B*, 2005, **106**, 563–571.
33 P. Ágoston, K. Albe, R. M. Nieminen and M. J. Puska, *Phys. Rev. Lett.*, 2009, **103**, 245501.
34 L. M. Huang, C. Århammar, C. Moysés Araújo, F. Silvearv and R. Ahuja, *Europhys. Lett.*, 2010, **89**, 47005.

35 A. Walsh, J. L. F. Da Silva and S.-H. Wei, *Phys. Rev. B: Condens. Matter Mater. Phys.*, 2008, **78**, 075211.
36 P. Hohenberg and W. Kohn, *Phys. Rev.*, 1964, **136**, B864.
37 W. Kohn and L. J. Sham, *Phys. Rev.*, 1965, **140**, A1133.
38 G. Kresse and J. Furthmüller, *Comput. Mater. Sci.*, 1996, **6**, 15.
39 G. Kresse and D. Joubert, *Phys. Rev. B: Condens. Matter Mater. Phys.*, 1999, **59**, 1758.
40 P. E. Blöchl, *Phys. Rev. B: Condens. Matter*, 1994, **50**, 17953.
41 H. J. Monkhorst and J. D. Pack, *Phys. Rev. B: Solid State*, 1976, **13**, 5188.
42 J. P. Perdew, K. Burke and M. Ernzerhof, *Phys. Rev. Lett.*, 1996, **77**, 3865.
43 P. Sherwood, A. H. de Vries, M. F. Guest, G. Schreckenbach, C. R. A. Catlow, S. A. French, A. A. Sokol, S. T. Bromley, W. Thiel, A. J. Turner, S. Billeter, F. Terstegen, S. Thiel, J. Kendrick, S. C. Rogers, J. Casci, M. Watson, F. King, E. Karlsen, M. Sjøvoll, A. Fahmi, A. Schäfer and C. Lennartz, *J. Mol. Struct.*, 2003, **632**, 1–28.
44 J. P. Perdew and M. Levy, *Phys. Rev. Lett.*, 1983, **51**, 1884.
45 L. J. Sham and M. Schlüter, *Phys. Rev. Lett.*, 1983, **51**, 1888.
46 M. Marsman, J. Paier, A. Stroppa and G. Kresse, *J. Phys.: Condens. Matter*, 2008, **20**, 064201.
47 J. Paier, M. Marsman and G. Kresse, *Phys. Rev. B: Condens. Matter Mater. Phys.*, 2008, **78**, 121201.
48 J. Heyd, G. E. Scuseria and M. Ernzerhof, *J. Chem. Phys.*, 2003, **118**, 8207–8215.
49 J. Muscat, A. Wander and N. M. Harrison, *Chem. Phys. Lett.*, 2001, **342**, 397–401.
50 I. de P. R. Moreira, F. Illas and R. L. Martin, *Phys. Rev. B: Condens. Matter Mater. Phys.*, 2002, **65**, 155102.
51 T. Bredow and A. R. Gerson, *Phys. Rev. B: Condens. Matter Mater. Phys.*, 2000, **61**, 5194.
52 F. Corà, M. Alfredsson, G. Mallia, D. S. Middlemiss, W. C. Mackrodt and R. Orlando, *Struct. Bonding*, 2004, **113**, 171–232.
53 A. Walsh, J. L. F. Da Silva, Y. Yan, M. M. Al-Jassim and S.-H. Wei, *Phys. Rev. B: Condens. Matter Mater. Phys.*, 2009, **79**, 073105.
54 D. O. Scanlon, B. J. Morgan, G. W. Watson and A. Walsh, *Phys. Rev. Lett.*, 2009, **103**, 096405.
55 J. Vidal, F. Trani, F. Bruneval, M. A. L. Marques and S. Botti, *Phys. Rev. Lett.*, 2010, **104**, 136401.
56 S. Chen, X. G. Gong, A. Walsh and S.-H. Wei, *Appl. Phys. Lett.*, 2009, **94**, 041903.
57 J. Paier, R. Asahi, A. Nagoya and G. Kresse, *Phys. Rev. B: Condens. Matter Mater. Phys.*, 2009, **79**, 115126.
58 J. Paier, M. Marsman, K. Hummer, G. Kresse, I. C. Gerber and J. G. Angyan, *J. Chem. Phys.*, 2006, **124**, 154709.
59 P. W. Tasker, *J. Phys.: Condens. Matter*, 1979, **12**, 4977.
60 X. Xia, R. Oldman and C. R. A. Catlow, *Chem. Mater.*, 2009, **21**, 3576–3585.
61 P. M. Oliver, S. C. Parker and W. C. Mackrodt, *Modell. Simul. Mater. Sci. Eng.*, 1993, **1**, 755.
62 C. Muggelberg, M. R. Castell, G. A. D. Briggs and D. T. Goddard, *Appl. Surf. Sci.*, 1999, **142**, 124–128.
63 M. Marezio, *Acta Crystallogr.*, 1966, **20**, 723–728.
64 O. Bierwagen, M. E. White, M. Y. Tsai and J. S. Speck, *Appl. Phys. Lett.*, 2009, **95**, 3.
65 G. Wulff, *Z. Kristallogr. Mineral.*, 1901, **34**, 449–530.
66 K. H. L. Zhang, A. Walsh, C. R. A. Catlow, V. Lazarov and R. G. Egdell, *Nano Lett.*, 2010, DOI: 10.1021/nl102403t, in press.
67 C. Korber, V. Krishnakumar, A. Klein, G. Panaccione, P. Torelli, A. Walsh, J. L. F. Da Silva, S.-H. Wei, R. G. Egdell and D. J. Payne, *Phys. Rev. B: Condens. Matter Mater. Phys.*, 2010, **81**, 165207.
68 A. Walsh, J. L. F. Da Silva, S.-H. Wei, C. Korber, A. Klein, L. F. J. Piper, A. DeMasi, K. E. Smith, G. Panaccione, P. Torelli, D. J. Payne, A. Bourlange and R. G. Egdell, *Phys. Rev. Lett.*, 2008, **100**, 167402.
69 J. F. Janak, *Phys. Rev. B: Condens. Matter*, 1978, **18**, 7165.
70 C. Di Valentin, G. Pacchioni and A. Selloni, *J. Phys. Chem. C*, 2009, **113**, 20543.
71 A. Walsh and C. R. A. Catlow, *ChemPhysChem*, 2010, **11**, 2341–2344.
72 J. L. F. Da Silva, M. V. Ganduglia-Pirovano, J. Sauer, V. Bayer and G. Kresse, *Phys. Rev. B: Condens. Matter Mater. Phys.*, 2007, **75**, 045121.
73 A. Walsh, J. L. F. Da Silva and S.-H. Wei, *Chem. Mater.*, 2009, **21**, 5119–5124.